



**HAL**  
open science

# Buckling of thick elasto-visco-plastic egg shells under external pressure: Experiments and bifurcation analysis

Nicolas Jacquet, Nicolas Tardif, Thomas Elguedj, Christophe Garnier

## ► To cite this version:

Nicolas Jacquet, Nicolas Tardif, Thomas Elguedj, Christophe Garnier. Buckling of thick elasto-visco-plastic egg shells under external pressure: Experiments and bifurcation analysis. *International Journal of Solids and Structures*, In press, 10.1016/j.ijsolstr.2022.111591 . hal-03637577v2

**HAL Id: hal-03637577**

**<https://hal.science/hal-03637577v2>**

Submitted on 11 Jul 2022

**HAL** is a multi-disciplinary open access archive for the deposit and dissemination of scientific research documents, whether they are published or not. The documents may come from teaching and research institutions in France or abroad, or from public or private research centers.

L'archive ouverte pluridisciplinaire **HAL**, est destinée au dépôt et à la diffusion de documents scientifiques de niveau recherche, publiés ou non, émanant des établissements d'enseignement et de recherche français ou étrangers, des laboratoires publics ou privés.

# Buckling of thick elasto-visco-plastic egg shells under external pressure: Experiments and bifurcation analysis

Nicolas Jacquet<sup>a,b,\*</sup>, Nicolas Tardif<sup>a</sup>, Thomas Elguedj<sup>a</sup>, Christophe Garnier<sup>b</sup>

<sup>a</sup>Univ Lyon, INSA-Lyon, CNRS UMR5259, LaMCoS, F-69621, France

<sup>b</sup>CEA-DES-IRENE-DTN Cadarache F-13108 Saint-Paul-Lez-Durance, France

---

## Abstract

*The buckling of rate dependent structures is not a topic often discussed in the literature. Methods to predict the buckling of such structures exist, but only few experimental works have been published, and even less when considering thick shell structures. In this work we are interested in the buckling of thick elasto-visco-plastic hemi-egg shells. We follow a modeling/experimental approach to analyse such problem. Buckling experiments at room temperature on hemi-egg shells subjected to external pressure are performed. 3D digital image correlation is used to measure the displacement fields on the inner surface of the hemi-egg shell during the buckling experiments. Due to the specimen shape and their loading, they experience non-proportional load paths. The effect of a non-proportional load path on the buckling behaviour has already been discussed many times in the literature for elasto-plastic materials. This work also intends to assess this point for a rate dependent material. A buckling prediction model is used to predict the buckling of hemi-egg shells. This model couples Bodner's approach with the deformation theory. It is used to estimate the buckling critical times and the buckling modes based on a preliminary finite element analysis. The effects of geometrical and loading imperfections on the buckling behaviour of the hemi-egg shells are also discussed. Finally, the experimental results are compared to the buckling predictions. A good correlation is observed between numerical results and experiments.*

*Keywords:*

Elasto-visco-plastic, buckling, finite element, bifurcation, experiment, DIC, FEMU

---

## 1. Introduction

The safety of nuclear reactors is a major issue. During the design process of a reactor, the integrity of the structural components is assessed. The mechanical loading is not the only input in the design of the structural components. The environmental conditions need to be considered as well, as they can be extreme in nuclear reactors, especially for a sodium fast reactor.

In such reactors and in particular locations, such as in the heat exchanger, the structural components can be exposed to high pressure and high temperature (more than 520°C). Because of their shapes and the external pressure applied on them, the buckling of some structural components has been identified as a failure case under ultimate loading. Under this thermal environment and because of the material used (316L(N) stainless steel), the rate-dependency of the material must be considered in the buckling analysis.

The buckling of rate dependent material is rarely investigated in the literature. Some authors, such as [Combescure and Jullien \(2017\)](#), [Papiro and Goldman \(1969\)](#), [Sammari and Jullien \(1995\)](#), experimentally investigated the buckling behaviour of shells with rate dependent materials. It is often focused on thin structures, one of the rare articles considering thick shell is [Gerard and Gilbert \(1958\)](#). In many cases, empirical buckling criterion are applied.

On the other hand, purely numerical articles were dedicated to the development of general criteria to predict buckling of rate dependent structures. Two main methods emerged from the literature. The first one was developed in [Bodner et al. \(1991\)](#). *Bodner* assumes that the strain rate stays constant at buckling, therefore an instantaneous plasticity problem can be defined and existing buckling criteria for rate independent materials can be used. The second method is more sophisticated, it is based on a sufficient condition of stability described in [Triantafyllidis et al. \(1997\)](#).

*Bodner's* hypothesis has been implemented for the buckling of thin shell in many article such as [Paley and Aboudi \(1991\)](#), [Mikkelsen \(1993\)](#) or [Eslami and Shariyat \(1997\)](#). *Bodner's*

---

\*Corresponding author.

*Email address:* nicolas.jacquet@insa-lyon.fr (Nicolas Jacquet)

hypothesis was also implemented in a previous article (cf. [Jacquet et al. \(2021\)](#)), where a numerical strategy to predict the buckling of thick elasto-visco-plastic plates subjected to proportional loading was presented. In [Jacquet et al. \(2021\)](#), *Bodner's* hypothesis is coupled with the deformation theory to predict buckling of thick plates. As already observed in [Hutchinson \(1974\)](#) and experimented by [Bardi and Kyriakides \(2006\)](#); [Kyriakides et al. \(2005\)](#); [Yeh and Kyriakides \(1986\)](#), any bifurcation analysis performed with a tangent moduli derived from any deformation theory gives better correlation with experiments than the one performed with a tangent moduli derived from the simplest incremental theory. A Good correlation between the buckling predictions and the experimental critical stresses and strains was found.

In this work we intend to evaluate the relevancy of the coupling of *Bodner's* assumption with the deformation theory for thick shells subjected to quasi proportional loadings.

The effect of the loading proportionality on the buckling behaviour of thick elasto-plastic shells is discussed in many articles (cf. [Tvergaard \(1983\)](#); [Tvergaard and Needleman \(2000\)](#); [Needleman and Tvergaard \(1982\)](#)). Different elasto-plastic constitutive models were also developed in order to take into account the effect of the loading non-proportionality on the tangent constitutive load (cf. [Christoffersen and Hutchinson \(1979\)](#); [Hughes and Shakib \(1986\)](#); [Simo \(1987\)](#)). These theories introduce additional material parameters to define non-smooth yield surfaces lowering the tangent stiffness and allowing a better correlation with buckling predictions. They are often called corner theories. In many cases, it is very difficult the define those additional material parameters physically. Indeed, the non-proportionality of the loading needs to be important in order to see a major difference with other theories such as the deformation theory. Moreover, [Budiansky \(2021\)](#) demonstrated that for quasi-proportional loadings, the slip theory (very similar to the corner theories) gives equivalent results that the deformation theory.

*Budiansky's* quasi-proportionality tolerance is discussed here with thick elasto-visco-plastic shells. In the present work, we also evaluate the buckling prediction model defines in [Jacquet et al. \(2021\)](#) for quasi-proportional loadings. Experimental results of buckling experiments performed on thick hemi-egg shells subjected to external pressure are presented

and analysed through Finite Element simulations. Bifurcation analyses are also performed on perfect and imperfect geometries. Imperfect boundary conditions are also considered.

In this article, the experimental methods and results are presented first. Then the numerical methods and results are introduced. Finally, both types of results are analysed, compared and discussed. The validity of *Budiansky's* quasi-proportional tolerance is also discussed for elasto-visco-plastic materials.

## 2. Experimental procedures

Because of the experimental constraints introduced by the testing at high temperature of buckling specimens made of 316L(N) stainless steel, it was chosen to use model material instead. This model material is a low melting point alloy (melting temperature: 217°C). Therefore, it is rate-dependent at room temperature. It allows to perform rate dependent buckling experiments at room temperature. This alloy is called Sn 3.0 Ag 0.5 Cu or SAC305. It is a Tin based alloy with 3.0% of silver and 0.5% of copper.

The shape and the manufacturing process of the buckling specimen are presented first. Then the bucking test rig and its instrumentation are introduced. Finally, the testing conditions are defined.

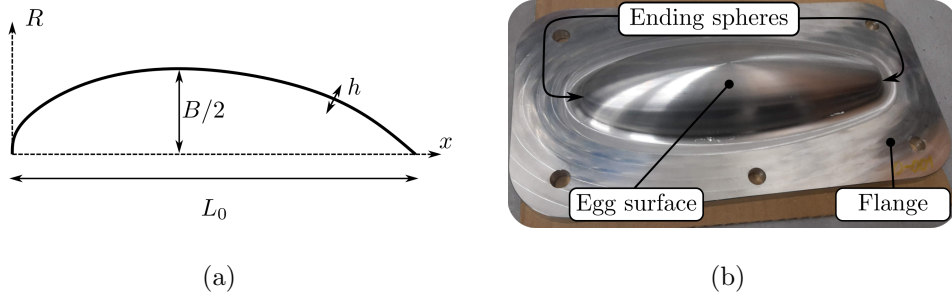
### 2.1. Specimen manufacturing

The buckling specimen designed is a hemi-egg shell. In order to position the buckling specimen in the test rig, a flange was added (cf. Figure 1(b)). The specimens were manufactured by gravity casting means. The flange and the hemi-egg shape were cast in one piece. The casting procedure followed is presented thereafter:

- Heating of the alloy and the mould to 280°C for at least 3h,
- Gravity casting of the alloy in the mould at room temperature,
- Rest for 1h at 250°C (in order to obtain a homogeneous temperature field in the mould),

- Water quench of the mould and its content (water temperature 40°C),
- Heat treatment for stress relieve, 1h at 100°C.

Following the casting process, the specimens were machined to their final shape by conventional milling processes.



**Figure 1:** (a) Egg geometry; (b) Egg specimen after machining

The hemi-egg shell shape of the specimen was defined from Zhang et al. (2017). It is defined by its major axis or length  $L$ , its minor axis or width  $B$  and its thickness  $h$ , as shown in Figure 1(a). The shape of the egg is defined by Zhang et al. (2017) as follows:

$$\text{for } x \in [0, L] : R(x) = \sqrt{L^{\frac{2}{n+1}} x^{\frac{2n}{n+1}} - x^2}, \quad (1)$$

with:

$$n = 1.057 \left( \frac{L}{B} \right)^{2.372}. \quad (2)$$

This shape is of interest, as it is a mixed shape between a cylinder and a sphere. When its aspect ratio  $L/B$  is equal to 1, we have a spherical egg, when  $L/B \rightarrow \infty$  the egg tends to be an infinite cylinder. This mixed shape presents a good buckling strength. It means that this shape is more likely to buckle in the inelastic range. Moreover, the loss of the second symmetry (compared to a sphere or a cylinder) allows to get a more complex buckling behaviour.

The egg shape is characterised by the  $B/L$  ratio, called the aspect ratio. As every axisymmetrical geometry, its thickness ratio can be defined by the  $R/h$  ratio.

The following shape parameters were chosen:  $L = 220$  mm,  $B = 66$  mm and  $h = 3$  mm. Therefore, the aspect ratio  $B/L$  is equal to 0.3 and the maximum value of the thickness ratio is equal to 11. The egg shell can be considered as thick.

In total five specimens were manufactured and tested. Because of ageing constraints, the specimens were tested less than 10000 hours (59.5 weeks) after casting. It insures no ageing effect on the mechanical properties (cf. [Dompierre et al. \(2011\)](#)). Table 1 summarises all the specimen produced, their quenching temperature and their dates of casting and testing.

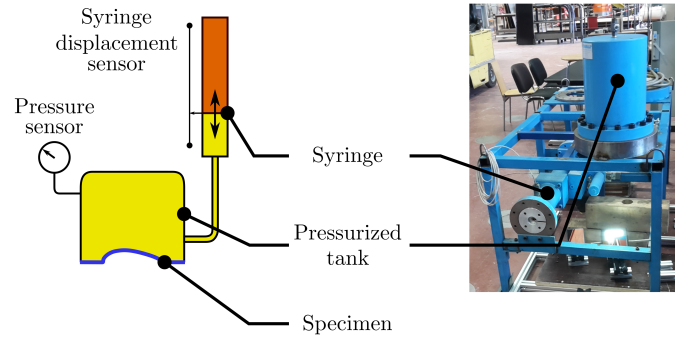
Specimen	Quench $T^\circ$ [°C]	Date of casting	Date of testing
O/002	20	11/2019	08/2020
O/003	40	06/2020	08/2020
O/004	40	06/2020	08/2020
O/005	40	07/2020	09/2020
O/006	40	07/2020	09/2020

**Table 1:** Produced specimens and their manufacturing history

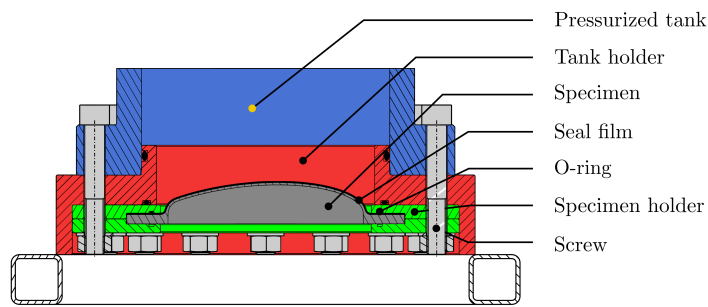
## 2.2. Test rig

The buckling experiments were performed on a test rig specially developed to test the buckling strength of shells subjected to external pressure. It was already used in [Sammari and Jullien \(1995\)](#). The test rig is composed of a pressurised tank filled with oil and closed by the specimen. The oil within the tank is pressurised by a syringe. The pressure is controlled through the displacement of the syringe piston. A 250 bars pressure sensor measures the pressure within the tank. Figure 2(a) presents the test rig pressurisation concept as well as a picture of the experimental set-up.

Sealing is an important issue for pressurised systems. As the specimen is part of the sealing system, special components were designed and manufactured to ensure optimal sealing performances of the rig. The assembly used to close the pressurised tank is presented in Figure 2(b).



(a)



(b)

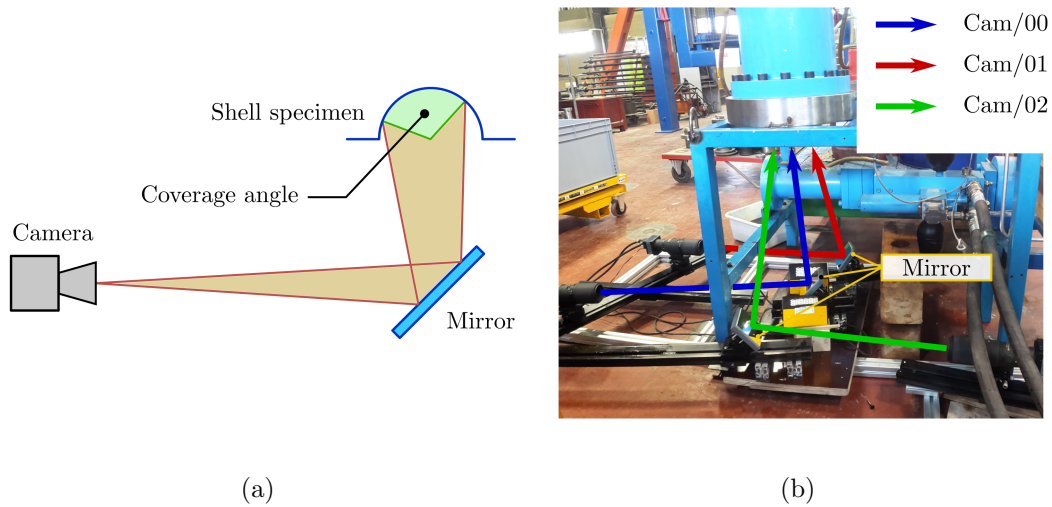
**Figure 2:** (a) Test rig pressurisation concept; (b) Test rig assembly with the specimen

The specimen is positioned between two specimen holders (in green in Figure 2(b)), an O-ring ensures sealing between the specimen and the upper specimen holder. This sub-assembly is then assembled to the tank thanks to 17 screws, tightened to 200 N.m as shown in Figure 2(b). In addition, an elastomer film covers the upper surface of the specimen to prevent any leakage due to material failure after buckling.

The displacement fields on the inner surface of the egg are measured by 3D-DIC means thanks to three cameras. The cameras work in couples to cover the largest region of interest, one camera is shared between the two couples of cameras used to perform the 3D-DIC. The specimen inner surface is covered by a speckle pattern characterised by a Gaussian distribution of its grey level. The grey level is coded on 8 bits. Each pixel takes a value between 0 and 255. The Gaussian distribution is defined by its mean value, 133 and its standard deviation 48. Each black pattern measures between 2 and 20 px.



In order to obtain the largest depth of field and the largest region of interest (ROI) on the inner surface of the hemi-egg shell, three 12 MPx cameras with 200 mm lenses were coupled to three 100 x 100 mm<sup>2</sup> mirrors. Each camera works with a single mirror, as illustrated in Figure 3(a). The three cameras are positioned within the test rig environment as depicted in Figure 3(b).



**Figure 3:** (a) Concept of indirect image acquisition; (b) Integration of the optical set-up in the test rig environment

The set-up of the cameras and the mirrors, and the configuration of the lenses allow to reach a depth of field of 20.5 mm. It corresponds to a total coverage angle of 140° (cf. Figure 3(a)).

Prior to any experiment, an evaluation of the displacement measurement uncertainty is performed. The uncertainty is analysed on the entire DIC ROI and for both couples of cameras. It is derived from a set of images captured when no loading was applied on the specimen. The characteristics of the normal distribution used to describe the displacement measurement uncertainty for both couples of cameras and for each experiment are presented in Table 2.

The uncertainty on the displacement measurement is satisfying according to the curved shape of the hemi-egg shell and the amplitude of the displacement field measured (cf. 3).

O/00#	Cameras 0 and 1		Cameras 0 and 2	
	Mean	StD	Mean	StD
	$\mu\text{m}$	$\mu\text{m}$	$\mu\text{m}$	$\mu\text{m}$
2	-5	17	2	12
3	-2	8	1	7
4	3	8	4	13
5	-8	8	3	8
6	-2	10	-1	12

**Table 2:** Statistical parameters of the accuracy of the DIC displacement fields

Because of the test rig set-up, it was not possible to measure accurately the initial geometric imperfection. Indeed, the initial geometric imperfection should have been measured once the specimen was set in the test rig. The only means would have been by DIC analysis. As seen previously, the uncertainty defined did not allow to characterise with accuracy the initial geometric imperfection.

### 2.3. Experimental conditions

The experiments were pseudo controlled in pressure. Full pressure controlled experiments were not possible as the rig was not designed to be controlled safely in pressure. Therefore, a pressure versus syringe displacement law was defined experimentally in order to apply the required pressure history to the specimen.

The pressure history is a saturating exponential law. It is defined by the following equation:

$$P(t) = P_{inf} \left( 1 - e^{-\frac{t}{t_{ref}}} \right). \quad (3)$$

The kinematic of the load is defined through the parameter  $t_{ref}$  (the reference time), while its amplitude is defined by  $P_{inf}$  (the saturating pressure). The targeted test conditions are presented in Table 3.

Specimen ID	L [mm]	B/L	h [mm]	$P_{inf}$ [MPa]	$t_{ref}$ [s]
O/002	220	0.3	3.0	5.0	100
O/003	220	0.3	3.0	5.0	100
O/004	220	0.3	3.0	5.0	100
O/005	220	0.3	3.0	5.0	1000
O/006	220	0.3	3.0	5.0	1000

**Table 3:** Summary of egg geometries and testing conditions

The test rig was equipped with a 25 MPa pressure sensor. Thanks to this sensor, the targeted pressure profiles could be compared to the actual ones. New sets of pressure profile parameters were also defined according to the measurement of the pressure history.

The results of the experiments are presented and discussed in the next section.

### 3. Experimental results

Thanks to the instrumentation of the experiments, many data were collected. In order to evaluate the buckling behaviour of the hemi-egg shell tested, several post-processing were required. First, the raw data needed to be post-processed, the pressure histories and the images gathered. They are post-processed to define respectively theoretical pressure histories and the 3D displacement fields on the lower skin of the hemi-egg shells. Then, those preliminary data are analysed in order to define the experimental buckling characteristics (i.e. the critical values and the buckling modes).

#### 3.1. Preliminary post-processing

##### Definition of the theoretical pressure profiles.

The pressure histories were gathered for all experiments and synchronised with the images captured by the cameras. As the experiments were pseudo controlled in pressure a first operation consisted in identifying the real pressure history. Table 4 summarises the pressure history parameters for each experiment. For each specimen the pressure profile is

characterised by three parameters,  $P_{inf}$  and  $t_{ref}$  already introduced and  $t_0$ , corresponding to the effective experiment start time. This identification is also characterised by its discrepancy. In Table 4, the parameters of the minimum and maximum envelop of the pressure measurement are added to the ones corresponding to the mean pressure profile identified.

O/00#	Target		Min.			Mean.			Max.		
	$P_{inf}$	$t_{ref}$	$P_{inf}$	$t_{ref}$	$t_0$	$P_{inf}$	$t_{ref}$	$t_0$	$P_{inf}$	$t_{ref}$	$t_0$
	MPa	s	MPa	s	s	MPa	s	s	MPa	s	s
2	5	100	4.71	53.4	162.3	4.70	52.4	160.9	4.67	50.7	159.2
3	5	100	5.02	89.7	70.8	5.01	90.4	66.9	4.96	89.5	61.2
4	5	100	4.67	104.4	54.9	4.58	100.6	51.6	4.55	100.4	47.2
5	5	1000	4.35	683.5	179.4	4.47	745.7	134.0	4.40	721.8	104.7
6	5	1000	4.35	691.9	142.4	4.40	722.6	108.7	4.35	707.8	81.1

**Table 4:** Identified pressure profile parameters

In order to better analyse all experiments, the pressure and the time are normalized as follows:

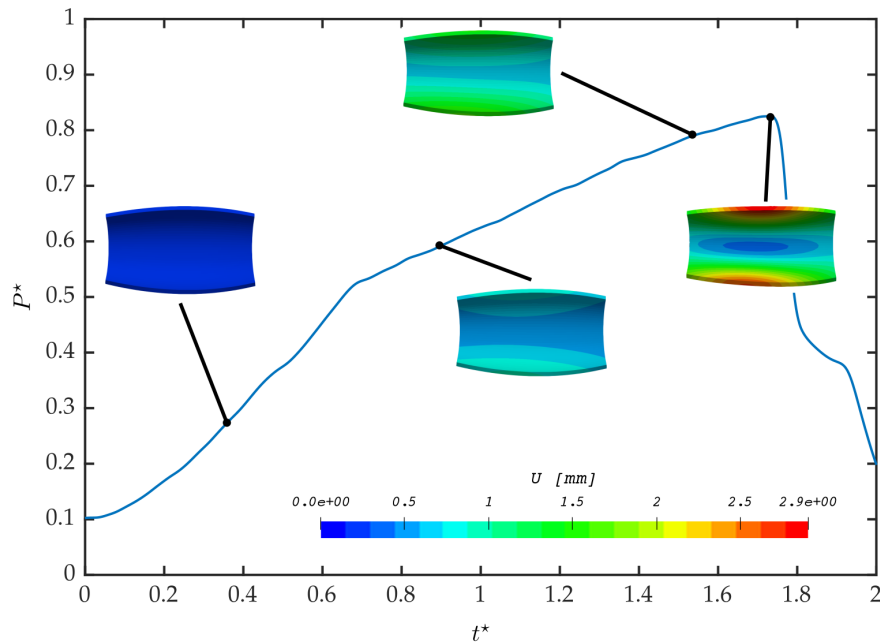
$$\begin{aligned}
 P^* &= P/P_{inf}, \\
 t^* &= (t - t_0)/t_{ref},
 \end{aligned}
 \tag{4}$$

with  $P^*$  the normalized pressure and  $t^*$  the normalized time.

### 3D-DIC of the images.

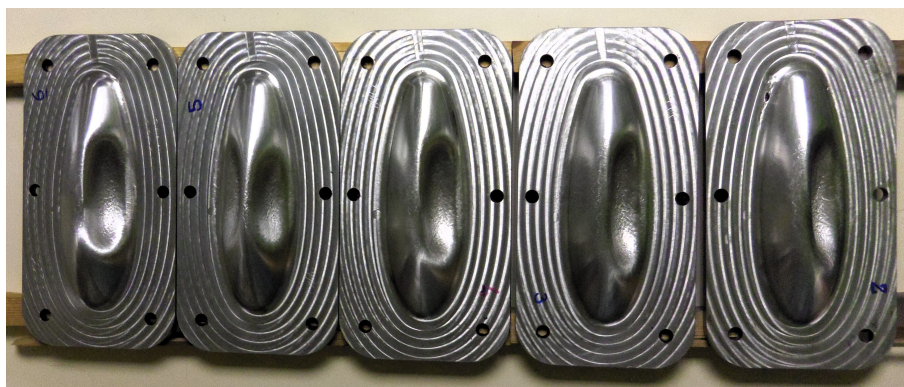
The images were post-processed with Ufreckles (a 3D-DIC software, cf. Réthoré (2018)) and a specific post-processing procedure in order to assemble the different sets of DIC data. For each experiment, the 3D displacement fields are defined on the ROI of the egg, as presented in Figure 4.

Figure 4 illustrates well the evolution of the egg shell deflection during an experiment. We first observe the lowering of the egg summit, followed by the development of two lobes,



**Figure 4:** Evolution of the egg ROI deflection with respect to the normalized time and pressure (O/003)

one on each side of the hemi-egg shell. In most of the cases, one lobe is preferred to the other at the collapse of the shell. For specimen O/005 a symmetric post buckling shape with two lobes was observed. Figure 5 presents the post buckling shape of all specimens tested.



**Figure 5:** Deformed specimens after buckling; from left to right: specimen O/006, O/005, O/004, O/003 and O/002

The post-processing of the displacement fields and the pressure histories also allow to define the measure uncertainties. They are then used in the definition of the critical value discrepancies.

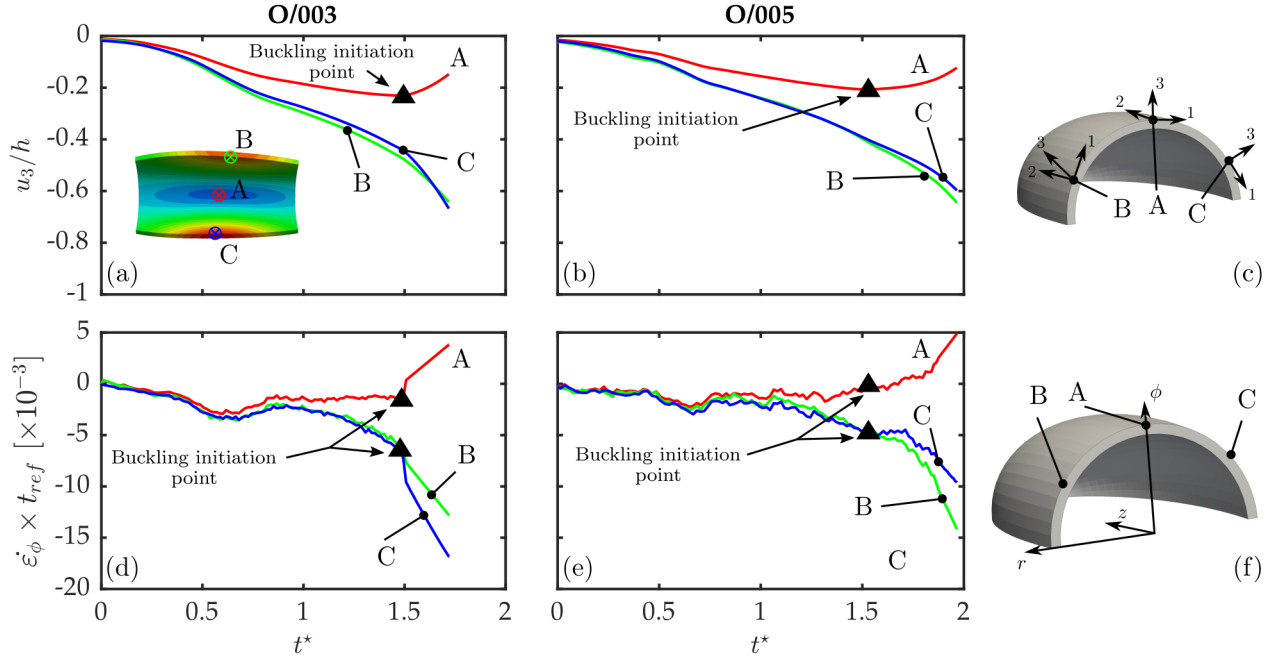
### 3.2. *Experimental buckling criteria*

The experimental buckling of a structure can be defined in many ways. First, the most common method is to associate the buckling to the maximum load (or collapsing load). This criterion is very efficient for rate independent materials. In the case of rate dependent materials, the strain rate increase introduced by the buckling can stiffen the structure, as opposed to rate independent materials. Because of this phenomenon, the global load can keep increasing even after bifurcation for rate dependent materials. This point was discussed in [Jacquet et al. \(2021\)](#). The maximum load therefore defines an upper bound of the bifurcation point.

Another approach consists in searching for any evidence showing the buckling initiation. In this work, it was chosen to analyse the out of plane displacement in the local coordinate system (1,2,3), where (1,2) plane is tangent to the egg inner surface, and the direction 3 is the normal to the surface, as shown in [Figure 6\(c\)](#). Three characteristic points were chosen to analyse the out of plane displacement, the egg summit (A), and the bottoms of both lobes (B) and (C) as indicated in [Figures 6\(c\) and 6\(e\)](#).

Two different specimens, presenting different post buckling shapes, were selected (i.e. specimen O/003 and O/005). For both specimens, one can first observe the lowering of the egg summit before changing direction around  $t^* = 1.5$  (as depicted by the red curves in [Figures 6\(a\) and 6\(b\)](#)). This change of direction is also associated with a change of speed of the lobe development at points B and C, as depicted by the green and blue curves in [Figures 6\(a\) and 6\(b\)](#).

This change of speed can also be characterised by the evolution of the circumferential strain rate at points A, B and C. As observed in [Figures 6\(d\) and 6\(e\)](#), at the time corresponding to the inversion of the egg summit displacement direction (depicted with a triangle symbol), one can also observe an increase of the strain rate at points A, B and C.



**Figure 6:** Evolution of the local normalized out of plane displacement  $u_3$  and the normalized circumferential strain rate  $\dot{\epsilon}_\phi$  for three characteristic points and for two specimens

This change of strain rate is associated to the buckling of the shell. This specific equilibrium point is considered as a lower bound of the buckling initiation. It is called inversion point in the rest of this document.

The maximum pressure point and the inversion point define an upper and a lower limit of the buckling phenomenon. The critical values and buckling modes are extracted at both equilibrium points in order to define a range of buckling likelihood.

### 3.3. Critical values

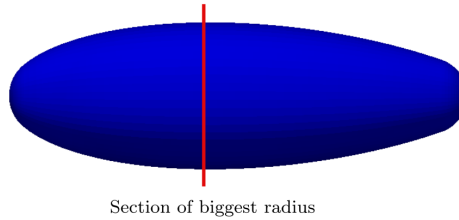
The properties of the inversion point and the maximum pressure point properties are summarised in Table 5 for all experiments. Their normalized values  $P_c^*$  and  $t_c^*$  can be defined according to the different pressure profile scenario presented in Table 4.

O/00#	Inversion point		Max. pressure point		Testing temp. °C
	$P_c$ MPa	$t_c - t_0^{mean}$ s	$P_{max}$ MPa	$t_{max} - t_0^{mean}$ s	
2	3.85	90.2	4.17	112.0	27
3	3.90	135.1	4.14	155.8	28
4	3.72	169.4	3.96	206.9	26
5	3.52	1146	3.65	1454	24
6	3.52	1142	3.71	1348	23

**Table 5:** Properties of the inversion point and the maximum pressure point

### 3.4. Buckling modes

Finally, the buckling modes can be extracted at the inversion point and at the maximum pressure point for each specimen. A Fast Fourier Transformation (FFT) is performed on the experimental displacement field at the section of biggest radius ( $R(x) = B/2$ , cf Figure 7). The FFT is used to isolate the trivial solution from the total one. When isolated, the trivial solution can be removed from the total one and the displacement solution responsible for the buckling of the structure can be characterised.

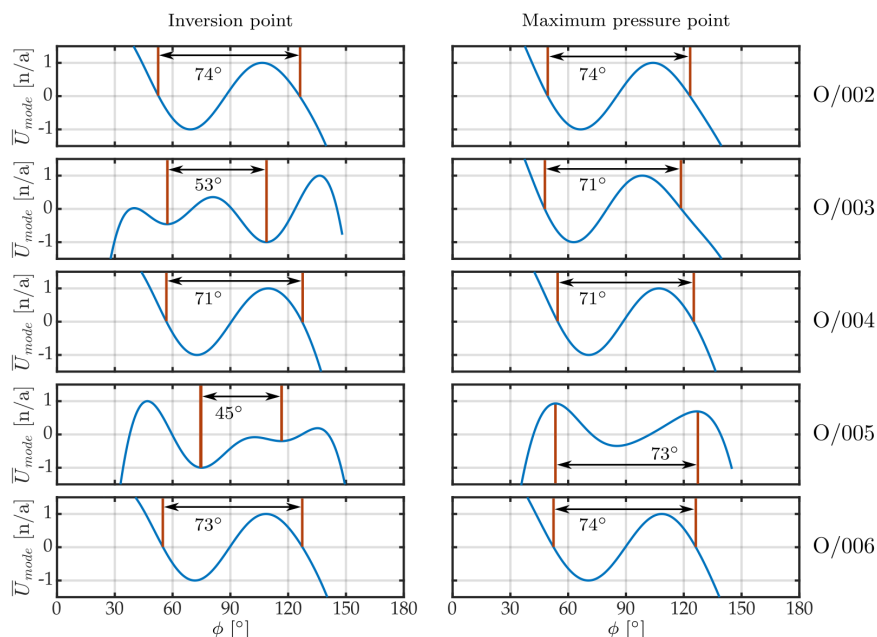


**Figure 7:** Position of the section of biggest radius along the egg axis

The first harmonic was identified as the elastic and plastic trivial displacements. It is removed from the solution in order to visualise an approximation of the buckling mode. The normalized buckling modes are presented in Figure 8 at the inversion point and at the maximum pressure point. They are plotted in a cylindrical reference frame as in Figure 6(f).



The FFT was performed on a sub-domain of the total egg, corresponding to the DIC ROI. Therefore, only a reduced part of the buckling mode is visible, mostly contained between  $60^\circ$  and  $120^\circ$ . Despite the usage of three cameras, the range of confidence in the ROI is reduced, indeed the DIC measurement close to the edges of the ROI is inaccurate.



**Figure 8:** Normalized buckling modes on the section of biggest radius for all specimens at the buckling initiation point and at the maximum pressure point

For most of the specimens, the buckling mode is asymmetrical at the maximum pressure point, except for specimen O/005 as already identified earlier. At the inversion point, one can observe perturbed buckling modes for specimens O/003 and O/005 and asymmetrical ones for the other specimens.

Symmetrical and asymmetrical modes share the same wave length between  $71^\circ$  and  $74^\circ$ , as shown in Figure 8 (right).

The presence of two different buckling modes at the maximum pressure point (upper bound of the bifurcation) and the proximity of the critical values (especially between specimens O/005 and O/006, which were tested under similar conditions) shows that at least the

first two modes are close. This is also confirmed by the perturbed modes observed at the inversion point. Indeed, the so-called perturbed modes of specimens O/003 and O/005 are a combination of the symmetrical and asymmetrical buckling modes identified at the maximum pressure point. Because of the proximity of the buckling modes, the structure can hesitate on which mode to buckle, as discussed in [Gerard and Gilbert \(1958\)](#).

The evolution of both displacement solutions (i.e. symmetrical or asymmetrical), from the pre-buckling regime to the post-buckling one, can be observed in [Figure 6](#). For specimen O/005 the post-buckling displacement field stays symmetrical, the radial displacement at points B and C changes speed but the curves stay parallel. For specimen O/003 the radial displacement at point C increases faster. It is due to the loss of symmetry of the post-buckling displacement solution. The loss of symmetry can also be seen at point A (i.e. the summit of the egg), for specimen O/003 the radial displacement at point A returns faster to zero than for specimen O/005 (i.e. with a symmetrical buckling mode).

This mode proximity is a good point to evaluate the relevancy of the prediction model. It is discussed in [Section 6](#).

#### **4. Numerical methods**

The numerical modelling of this buckling problem can be approached in two different ways and with different objectives.

The first one consists in performing a bifurcation analysis on the perfect hemi-egg shells. This approach allows to generate buckling predictions. These predictions include: the predicted critical values (pressure, time, etc...) and the predicted buckling modes.

On the other hand, the finite element simulation of each experiment can be used in order to identify the yield stress of each specimen and to validate the good agreement of the material constitutive model with the experiments.

In both approaches, the material constitutive model has an important effect on the results. For this reason, the material constitutive model used in this work is briefly presented. Then the numerical approach to generate buckling predictions is introduced. Finally, the finite element modelling of each buckling experiment is described.

#### 4.1. Material constitutive model

The material behaviour of the SAC 305 alloy is modelled with a unified elasto-viscoplastic model. The creep behaviour is modelled with a Norton law and the isotropic hardening with three Voce hardening parameters. The transverse isotropy of the SAC 305 is modelled with *Hill's* yield criterion. It was chosen to keep elasticity isotropic. The constitutive law is defined by the following set of equations:

$$\begin{aligned}
\boldsymbol{\sigma} &= \mathbf{C} \boldsymbol{\varepsilon}_e, \\
\boldsymbol{\varepsilon} &= \boldsymbol{\varepsilon}_e + \boldsymbol{\varepsilon}_p, \\
\dot{p} &= g(f) = \left( \frac{f}{K} \right)^n, \\
f &= \sigma_{eq} - R(p), \\
R(p) &= R_0 + \sum_{i=1}^3 R_i (1 - e^{-b_i p}), \\
\sigma_{eq} &= \sqrt{\boldsymbol{\sigma} : \mathbf{H} : \boldsymbol{\sigma}},
\end{aligned} \tag{5}$$

with,  $\boldsymbol{\sigma}$  the Cauchy stress tensor,  $\boldsymbol{\varepsilon}$  the Biot strain tensor,  $\boldsymbol{\varepsilon}_e$  the elastic strain tensor and  $\boldsymbol{\varepsilon}_p$  the plastic strain tensor,  $\mathbf{C}$  the isotropic elastic linear operator,  $\sigma_{eq}$  *Hill's* equivalent stress defining the yield surface,  $\mathbf{H}$  the Hill tensor (used here for transverse anisotropy),  $p$  the equivalent plastic strain,  $R$  the hardening variable and  $\dot{p}$  the equivalent strain rate.

In the general case *Hill's* tensor is defined by:

$$\mathbf{H} = \begin{bmatrix} F + H & -F & -H & 0 & 0 & 0 \\ -F & G + F & -G & 0 & 0 & 0 \\ -H & -G & H + G & 0 & 0 & 0 \\ 0 & 0 & 0 & L & 0 & 0 \\ 0 & 0 & 0 & 0 & M & 0 \\ 0 & 0 & 0 & 0 & 0 & N \end{bmatrix}. \tag{6}$$

In case of transverse isotropy, *Hill's* tensor is completely defined by the Lankford coefficient  $R_{Lank}$  as follows:

$$F = \frac{R_{Lank}}{R_{Lank}+1} \quad G = \frac{1}{R_{Lank}+1} \quad H = \frac{1}{R_{Lank}+1} \quad L = \frac{3}{2} \quad M = \frac{3}{2} \quad N = \frac{3}{2} \tag{7}$$

and:

$$R_{Lank} = \varepsilon_{pp}/\varepsilon_{zz}, \quad (8)$$

with  $\mathbf{p}$  any vector of the plane tangent to the shell and  $\mathbf{z}$  its thickness direction.

The material parameters are  $R_0$ ,  $R_1$ ,  $b_1$ ,  $R_2$ ,  $b_2$ ,  $R_3$ ,  $b_3$ ,  $K$ ,  $n$ ,  $R_{lank}$  and  $\mathcal{C}$  defined by Young's modulus and the Poisson ratio.

The identification of the material parameters was presented in [Jacquet et al. \(2021\)](#) and [Jacquet \(2021\)](#). This identification was performed using tensile test experiments and a Finit Element Model Updating (FEMU) approach. Tensile experiments were performed on a specific specimen geometry and at different strain rates. It allows to identify the material parameters on three decades of strain rate (cf. [Jacquet et al. \(2021\)](#)). As mentioned in [Kim et al. \(2002\)](#), the SAC305 alloy behaviour is dependent of the cooling rate at solidification. This dependency affects the material properties through the yield stress almost exclusively. Therefore, the value of the yield stress needs to be defined for each specimen.

The [Table 6](#) summarises the material parameters associated to the mean material laws. This law is used later for all FE simulations.

Parameters	$R_0$	$R_1$	$b_1$	$R_2$	$b_2$	$R_3$	$b_3$	$K$	$n$	$R_{Lank}$	$E$	$\nu$
Values	TbD	8.5	395.2	5.2	28.8	8.3	2134.2	2133.8	2.9	1.18	41513	0.35
Units	MPa	MPa	n/a	MPa	n/a	MPa	n/a	MPa.s <sup>1/n</sup> /a	n/a	n/a	MPa	n/a

**Table 6:** Parameters of the mean reference law (TbD:To be defined in [Section 5.1.1](#))

It is identified thanks to an inverse method using the experimental data from the beginning of each experiment. The results of this analysis are presented in [Section 5.1.1](#).

#### 4.2. Bifurcation analysis

The buckling prediction model is defined through the derivation of the tangent constitutive law. In this subsection the constitutive law is introduced first. Then, thanks to *Bodner's* hypothesis and the deformation theory, the tangent modulus can be derived. Finally, this modulus can be used in a FE model to perform the bifurcation analysis of a structure.

#### 4.2.1. Derivation of the tangent constitutive law

*Bodner's* hypothesis allows to write an instantaneous plastic problem by neglecting the strain rate variation at bifurcation. This is expressed by:

$$d\dot{p} = d(g(f)) = g'(f)df = 0, \quad (9)$$

where  $g$  is the visco-plastic law,  $f$  the yield criterion and  $\dot{p}$  the equivalent inelastic strain rate.

In the deformation theory, the plastic strain is proportional to the deviatoric stress tensor. The flow rule is defined as follows:

$$\boldsymbol{\varepsilon}^p = p \frac{\mathbf{H} \boldsymbol{\sigma}}{\sigma_{eq}}. \quad (10)$$

Its variational expression is then written as:

$$\dot{\boldsymbol{\varepsilon}}^p = \frac{\dot{\sigma}_{eq}}{\sigma_{eq}} \left( \frac{\dot{p}}{\dot{\sigma}_{eq}} - \frac{p}{\sigma_{eq}} \right) \mathbf{H} \boldsymbol{\sigma} + p \frac{\mathbf{H} \dot{\boldsymbol{\sigma}}}{\sigma_{eq}}. \quad (11)$$

Using the additive decomposition of the strain tensor and Equation 9, we can write:

$$\dot{\boldsymbol{\varepsilon}} = \left[ \mathbf{C}^{-1} + \frac{p}{\sigma_{eq}} \mathbf{H} + \left( \frac{\dot{p}}{\dot{\sigma}_{eq}} - \frac{p}{\sigma_{eq}} \right) \frac{\mathbf{H} \boldsymbol{\sigma} \otimes \mathbf{H} \boldsymbol{\sigma}}{\sigma_{eq}^2} \right] \dot{\boldsymbol{\sigma}}, \quad (12)$$

and therefore:

$$\mathbf{C}_t = \left[ \mathbf{C}^{-1} + \frac{p}{\sigma_{eq}} \mathbf{H} + \left( \frac{\dot{p}}{\dot{\sigma}_{eq}} - \frac{p}{\sigma_{eq}} \right) \frac{\mathbf{H} \boldsymbol{\sigma} \otimes \mathbf{H} \boldsymbol{\sigma}}{\sigma_{eq}^2} \right]^{-1}. \quad (13)$$

The tangent moduli  $\mathbf{C}_t$  includes the elasto-visco-plastic behaviour of the SAC 305 alloy as well as its transverse isotropic behaviour through  $\mathbf{H}$ , the Hill's tensor. The tangent moduli  $\mathbf{C}_t$  can then be used to compute the tangent stiffness matrix of a FE model. The tangent stiffness matrix is then used to perform the buckling analysis. This point is detailed in the next paragraph.

#### 4.2.2. Buckling prediction model

In this work the hemi-egg shell is modelled through the FE software Cast3M (cf. [CEA \(2018\)](#)). SHB8PS volume shell elements (cf. [Abed-Meraim and Combescure \(2009\)](#)) are

used. Thanks to the formulation of the SHB8PS, only one element is used in the thickness direction of the shell. Only the hemi-egg shell portion of the buckling specimen is considered, as illustrated in Figure 9(a). In the perfect case, the edges of the hemi-egg shell are perfectly clamped. Geometric or boundary condition imperfections can also be applied.

A prerequisite to the bifurcation analysis is to compute the trivial solution branch. For this purpose, a classical updated Lagrangian method is used.

The bifurcation analysis is then performed according to *Hill's* method, with the following eigenvalue problem:

$$\det [\mathbf{K}_{MAT} + \mathbf{K}_{BC} + \lambda (\mathbf{K}_{GEOM} + \mathbf{K}_{NL})] = 0, \quad (14)$$

where  $\mathbf{K}_{BC}$  corresponds to the Lagrange multiplier matrix,  $\mathbf{K}_{NL}$  is the matrix associated to the non-linear effect of the following pressure,  $\mathbf{K}_{GEOM}$  is the geometric stiffness matrix, and  $\mathbf{K}_{MAT}$  is the tangent stiffness matrix.

The structure bifurcates when the smallest eigenvalue gets smaller than 1, which corresponds to the singularity of the total tangent stiffness matrix ( $\mathbf{K}_{MAT} + \mathbf{K}_{BC} + \mathbf{K}_{GEOM} + \mathbf{K}_{NL}$ ). For this specific equilibrium, the critical time and pressure are extracted. In this work, we are especially interested in the critical time as it is more affected by the viscous behaviour and the buckling paradox than the critical pressure.

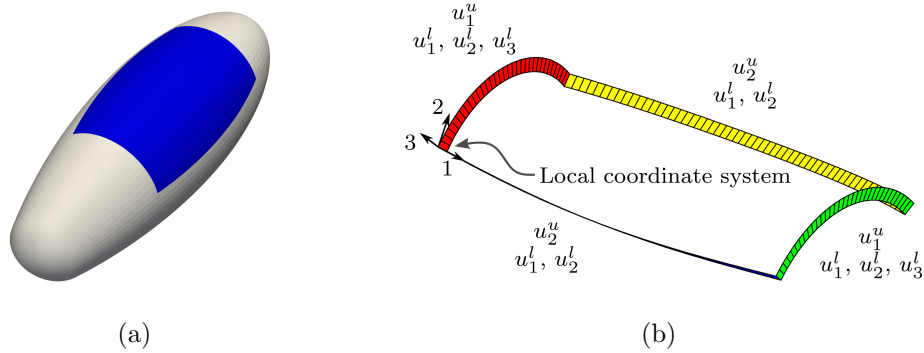
### 4.3. Modelling of the experiments

In order to identify the yield stress value for each experiment and to verify the validity of the other material parameters, a finite element model of each experiment was generated.

The geometry and the mesh of the FE model are derived from the DIC ROI. It is depicted in blue in Figure 9(a) and compared to the overall hemi-egg shell in grey.

The loading of the FE model is performed through the application of the experimental pressure on the outer skin (or upper skin) of the egg shell ROI, and the enforcement of boundary conditions on the egg shell ROI. The boundary conditions are directly taken from the DIC displacement fields for the lower skin. On the upper skin, the boundary conditions

are enforced using the DIC displacement fields of the lower skin and the Kirchhoff-Love shell kinematic assumption. They are enforced as mentioned in Figure 9(b).



**Figure 9:** (a) DIC ROI in the total hemi-egg shell geometry; (b) enforcement of the DIC boundary condition on the DIC ROI mesh ( $u_1$  and  $u_2$  are the displacement fields in the local frame with (1, 2) an plane tangent to the egg mid surface, with  $u$  for the upper skin and  $l$  for the lower skin),

The out of plane displacement on the lower (or inner) skin of the egg shell ROI can then be compared to the experimental displacement field from the DIC analysis. This quantity is used either for the identification of the yield stress value or the assessment of the constitutive model.


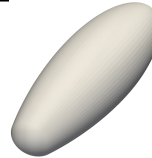
For the identification of the yield stress on each experiment, only the experimental data from the beginning of each experiment are used (before collapse of the egg shell).

The errors between the experimental and numerical displacement fields on the lower skin of the egg shell are also analysed to validate the good agreement of the other material parameters with the experiments. The material parameters (except than the yield stress) were identified previously (cf. [Jacquet et al. \(2021\)](#) and [Jacquet \(2021\)](#)).

This model can also be used in order to evaluate the experimental boundary condition imperfections. Indeed, comparing the displacement fields computed with this model to the ones obtained with the perfect hemi-egg, allows to identify the boundary condition imperfections introduced during the experiments. This analysis is discussed in Section 6.1.2.

Table 7 presents a summary of the models developed in the works. In the rest of this

document, the model numbering defined in Table 7 are used.

Models	Model 1	Model 2
Mesh	 DIC ROI (in blue)	 Hemi-egg
FE elements	SHB8PS	
B.C.	DIC disp.	Perfectly clamped
Load	Mean experimental pressure	Theoretical or mean experimental pressure
Material	Mean reference law and specimen yield stress (cf. Table 6)	

**Table 7:** Summary of FEA models

## 5. Numerical results

The present work intends to challenge an original buckling criterion against experimental data. In this section the results from the different numerical simulations are presented.

### 5.1. Simulation of the experiments

Before intending any validation of the buckling prediction model, it is required to assess the validity of the constitutive law for the type of loading and the specimen tested.

First the results of the yield stress identification procedure are presented. Then, the validity of the constitutive model and the identification of its parameters is assessed. Finally, comparing the displacement field from the simulation of the experiments (**Model 1**) with the displacement field from the analysis on the perfect hemi-egg shells (**Model 2**), the boundary condition imperfections can be identified.



### 5.1.1. Identification of the yield stress

As already mentioned, because of the SAC 305 cooling rate dependency and because of the size of the specimen ingots, the yield stress of each specimen needs to be identified. For this purpose an inverse method (using **Model 1**) was implemented to identify the yield stress ( $R_0$ ). The other material parameters were identified previously (cf. [Jacquet et al. \(2021\)](#) and [Jacquet \(2021\)](#)) and are summarised in Table 6. They are used and fixed in this identification process.

Only the pre-buckling phase of the experiments is used for the identification of the yield stress. The identified yield stress and the associated uncertainty range are presented for each specimen in Table 8.

O/00#	Mean $R_0$	Min. $R_0$	Max. $R_0$
	MPa	MPa	MPa
2	10.2	9.8	10.6
3	10.7	10.2	11.2
4	9.4	9.0	10.0
5	11.1	10.5	11.8
6	10.4	9.7	11.2

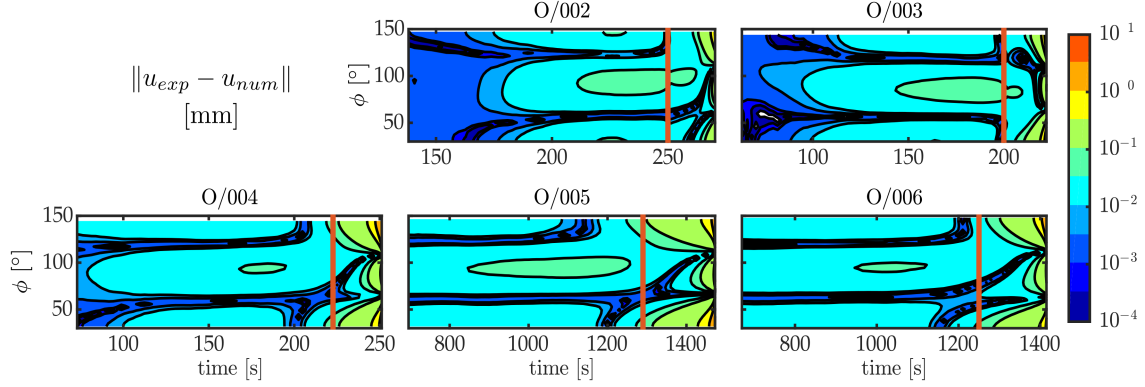
**Table 8:** Yield stress decrease identified in the pre-buckling phase

### 5.1.2. Validation of the constitutive material law

Following the identification of the yield stress ( $R_0$ ), the validity of the constitutive law identified in [Jacquet et al. \(2021\)](#) is assessed for this specific loading case.

The out of plane displacement field from the finite element simulation (computed with **Model 1**) is compared to the experimental out of plane displacement field for each experiment. The difference between both displacement fields is extracted on the section of biggest radius ( $R(x) = B/2$ ) and on the lower skin. The evolution of the difference is plotted in a

chronograph for each specimen in Figure 10.



**Figure 10:** Chronograph of the error on the out of plane displacement between experiments and simulations at the section of biggest radius for all specimens; the vertical red line corresponds to the inversion point (early stage of the buckling phenomenon)

One can see that the error between the simulation and the experiment is reasonable up to the initiation collapse of the egg (depicted with the vertical red line and corresponding to the inversion point). In the pre-collapse range, the displacement error is lower than 0.1 mm. This error is also mostly concentrated at the summit of the egg (i.e.  $\phi = 90^\circ$ ). This can be explained, as the displacement amplitude in this region is low (as shown in Figure 4). Therefore, any source of imperfection, material, geometric or boundary conditions can have an important impact on the amplitude of the displacement in this area of the egg shell.

Nevertheless, a good agreement of the finite element simulations of the experiment with the experimental data is observed. Therefore, the constitutive model and the identification of its parameters can be considered as satisfying.

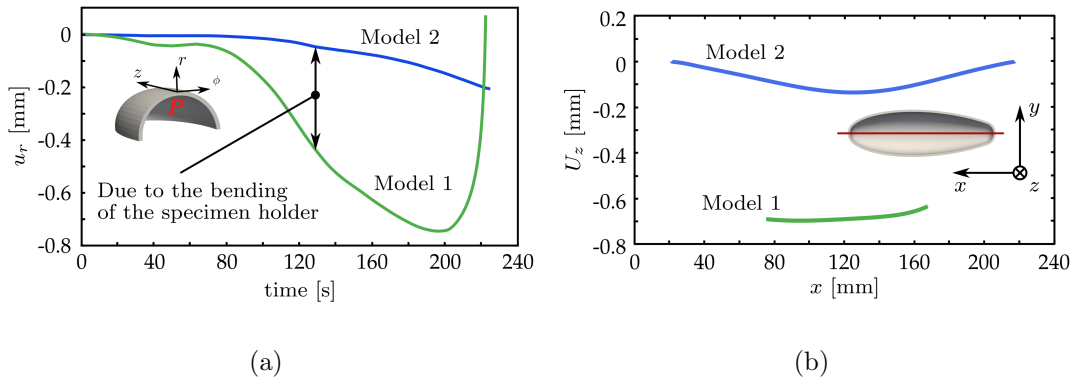
### 5.1.3. Experimental boundary condition imperfections

Thanks to the results obtained in the previous section, the boundary condition imperfections can be identified by comparing the numerical results from **Model 1** with the ones from **Model 2**. We have to be careful that the same loading condition is enforced (i.e. the

experimental pressure history).

As they are both using the same material and experiencing the same pressure, any difference between the results of **Model 1** and **Model 2** would show the effects of boundary condition imperfections.

To illustrate this point, the evolution of the out of plane displacement of the egg summit is plotted with respect to time for both models (i.e. **Model 1** and **Model 2**) in Figure 11(a).



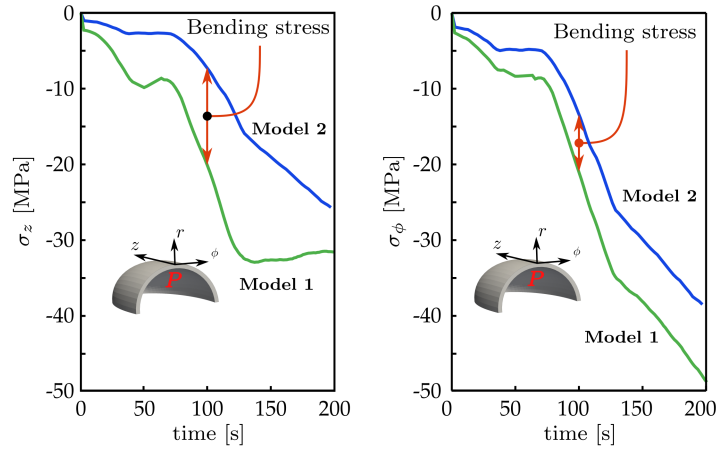
**Figure 11:** (a) Effect of the loading imperfection on the radial deflection  $u_r$  of a point (P) on the top on the egg (O/003), green **Model 1**, blue **Model 2**; (b) Effect of the loading imperfection on the vertical deflection  $U_z$  of an axial section of the lower skin (red line) of egg O/003), green **Model 1**, blue **Model 2**

As shown in Figure 11(a), the displacements extracted from the results of **Model 1** and **Model 2** diverge from the beginning of the experiment. This divergence is due to the bending of the specimen holders as well as the specimen flange. This bending deflection is due to the applied pressure. Indeed, in **Model 2** the hemi-egg is perfectly clamped, the point on the top of the egg only experiences the displacement due to the deflection of the egg.

In Figure 11(b) the vertical displacement (i.e.  $U_z$ ) of the axial section of the lower skin (red line in Figure 11(b)) is depicted for **Model 1** and **Model 2** at  $t = 200$  s. The displacement fields have different shapes. On **Model 2**, the deflection in the center due to

the pressure is well visible. On **Model 1**, the same deflection is embedded in the bending displacement field of the specimen holder. Therefore, the deformation is less localized in the center of the egg.

The bending moment applied to the egg during the experiment also affects the axial ( $\sigma_z$ ) and the circumferential ( $\sigma_\phi$ ) stress amplitudes as shown in Figure 12 for a point on the top of the egg.



**Figure 12:** Effect of the loading imperfection on the stress state for a point (P) at the top of the egg (O/003),  $\sigma_z$  the axial stress and  $\sigma_\phi$  the circumferential stress

The axial stress is more affected than the circumferential one as seen in Figure 12. As the egg buckles on a circumferential mode, it seems that the specimen holder bending does not affect the buckling behaviour of the shell. The effects of such loading imperfections are discussed in Section 6.1.

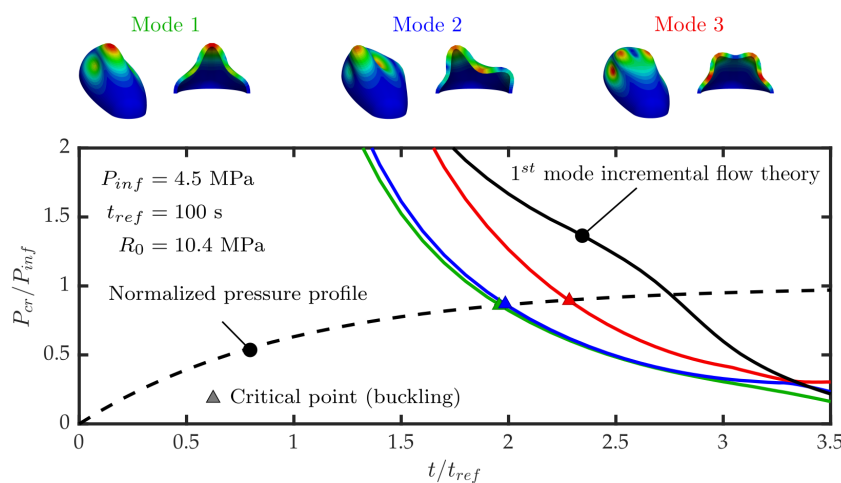
### 5.2. Buckling prediction on the perfect hemi-egg shell

Finally, the buckling prediction model is applied to the perfect hemi-egg shell (i.e **Model 2**), used with theoretical pressure histories. As a reminder, its edges are perfectly clamped. In this section, two reference load cases were selected. They are close to the ones identified in Section 3. They are characterised by  $P_{inf} = 4.5$  MPa and  $t_{ref} = 100$  and 1000 s. In

addition, the yield stress ( $R_0$ ) is set to 10.4 MPa. It corresponds to the mean value of the identified yield stress on the egg specimens (cf. Table 8).

### 5.2.1. Bifurcation analysis

The bifurcation analysis is performed through the solving of the eigenvalue problem defined in Equation 14. The bifurcation analysis allows to define the critical values for the first buckling modes as well as the shape of the buckling modes. Only the first three modes are extracted from the bifurcation analysis.



**Figure 13:** Illustration of the first three buckling modes defined through the deformation theory, and their eigen pressures according to the normalized time.

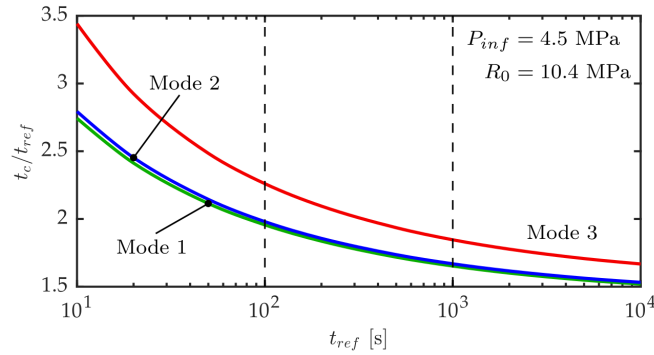
Figure 13 presents the results from the bifurcation analysis for  $t_{ref} = 100$  s and  $P_{inf} = 4.5$  MPa. In Figure 13 the evolution of the normalized eigen-pressure (i.e.  $\lambda \times P/P_{inf}$ ) are plotted with respect to time for the first three modes. They are depicted by the plain coloured lines. In addition, the evolution of the normalized pressure according to time is depicted by the dashed black line. The points corresponding to the intersection of the eigen-pressure curves with the pressure curve define the critical points for each buckling mode. As a reference, the eigen-pressure of the first buckling mode predicted with an incremental flow theory is also plotted with respect to time. It is depicted by the plain black line.

One can observe that the eigen-pressure curves of the first two modes (green and blue curves) are almost superimposed. It means that the first or the second mode can develop at the same pressure and at the same time. Moreover, they share the same buckling mode wave length, one peak and two valleys (cf. Figure 13). The first buckling mode shape is symmetrical while the second one is asymmetrical.

The third buckling mode is well separated from the first two modes. It should not intervene in the buckling behaviour of the hemi-egg shell.

The eigen-pressure of the first mode defined with an incremental flow theory is always higher than all other eigen-pressure curves. This is a well-known result for elasto-plastic materials (cf. Kyriakides et al. (2005)).

In addition, the evolution of the critical time ratio (time at buckling  $t_c$  divided by the reference time  $t_{ref}$ ) for the first three modes can be plotted with respect to the reference time  $t_{ref}$  in Figure 14. Each coloured line corresponds to a specific buckling mode: mode 1 in green, mode 2 in blue and mode 3 in red.



**Figure 14:** Evolution of the critical time ratios of the first three modes with respect to the reference time (deformation theory)

We can see that the critical time decreases when  $t_{ref}$  increases for all modes. This effect is due to the rate dependency of the material. Indeed, for high strain rates (i.e. low values of  $t_{ref}$ ), the strain rate increases slightly the tangent stiffness through the parameter  $\sigma_{eq}/p$  of Equation 13.

### 5.2.2. Proportionality of the loading at buckling

In this work we are also interested in the non-proportional character of the loading path. The proportionality of the load path can be defined in many different ways. In this work the convention from [Christoffersen and Hutchinson \(1979\)](#) was chosen. The proportionality of the load path is defined by the  $\theta$  variable. [Christoffersen and Hutchinson \(1979\)](#) define  $\theta$  as follows:

$$\cos \theta = \frac{(\mathcal{L}_p \mathbb{U}_\sigma) : \dot{\boldsymbol{\sigma}}}{(\dot{\boldsymbol{\sigma}}^t \mathcal{L}_p \dot{\boldsymbol{\sigma}})^{1/2}}, \quad (15)$$

with:

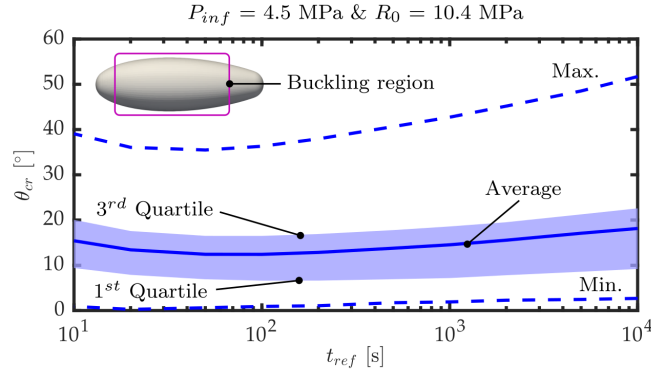
$$\mathbb{U}_\sigma = \frac{\mathbf{H} \boldsymbol{\sigma}}{(\boldsymbol{\sigma}^t \mathbf{H} \mathcal{L}_p \mathbf{H} \boldsymbol{\sigma})^{1/2}}, \quad \mathcal{L}_p = \frac{p}{\sigma_{eq}} \mathbf{H} + \left( \frac{\dot{p}}{\dot{\sigma}_{eq}} - \frac{p}{\sigma_{eq}} \right) \frac{\mathbf{H} \boldsymbol{\sigma} \otimes \mathbf{H} \boldsymbol{\sigma}}{\sigma_{eq}^2}. \quad (16)$$

The buckling predictions generated previously are only valid if the loading is quasi-proportional at buckling. Therefore, the value of  $\theta$  at buckling,  $\theta_{cr}$ , needs to be analysed. As the  $\theta$  field on the egg shell is heterogeneous, its range is analysed statistically in the buckling region of the egg shell (cf. [Figure 15](#)). In [Figure 15](#), the range of  $\theta$  at buckling is plotted with respect to the reference time  $t_{ref}$ . The shaded surface covers the second and third quartiles, the plain line corresponds to the average value of theta and dashed lines to the maximum and minimum values.

One can see that the range of  $\theta$  is reasonable. The upper bound of the third quartile is lower than  $20^\circ$  for  $t_{ref}$  lower than 2000 s. It means that for at least 75% of the buckling region, the value of  $\theta$  at buckling is lower than  $20^\circ$ . Nevertheless, one can see that the maximum value of the  $\theta$  range increases with  $t_{ref}$ , from less than  $40^\circ$  for  $t_{ref} = 100$  s to more than  $50^\circ$  for  $t_{ref} = 10000$  s. As there is only a limited number of points where the non-proportionality cannot be neglected, we can still assume that the loading is quasi proportional.

To summarise this buckling analysis, the critical values for the reference load cases are summarised in [Table 9](#).

To conclude on the bifurcation analysis of the perfect hemi-egg shell, we observed that the first two buckling modes are very close. It was also observed that the strain rate increases



**Figure 15:** Evolution of the range of  $\theta$  at buckling with respect to the reference time (deformation theory)

$P_{inf}$	$t_{ref}$	$P_c$	$t_c$	$\theta$ range				
				mean	max.	min.	1 <sup>st</sup> quartile	3 <sup>rd</sup> quartile
MPa	s	MPa	s	°	°	°	°	°
4.5	100	3.9	196	12.4	36.3	0.9	6.6	16.5
4.5	1000	3.6	1653	14.5	42.7	1.9	7.2	18.6

**Table 9:** Critical values for the two reference load cases

the critical time. Finally, the hypothesis of quasi-proportional loading was validated through the analysis of the range of  $\theta$  at buckling.

The results obtained at this stage constitute a reference set of data used later to validate the buckling prediction model. The effect of imperfections on this set of data is discussed in the next section.

## 6. Discussions

In the previous section, the experimental results as well as the numerical ones from **Model 1** and **Model 2** were presented. The relevancy of the constitutive model selected and identified was also observed. In addition, some sources of imperfection on the boundary



conditions were also identified. Finally, the results of a bifurcation analysis for two reference load cases were presented.

In this section, we first discuss the effect of the imperfection on the buckling behaviour of the hemi-egg shell. Then the validity of the original buckling criterion presented in Section 4.2 is discussed.

### 6.1. Effect of imperfections

In this work, two types of imperfections are considered. The ones introduced to the initial hemi-egg shell geometry and the ones introduced during the experiment through imperfect boundary conditions.

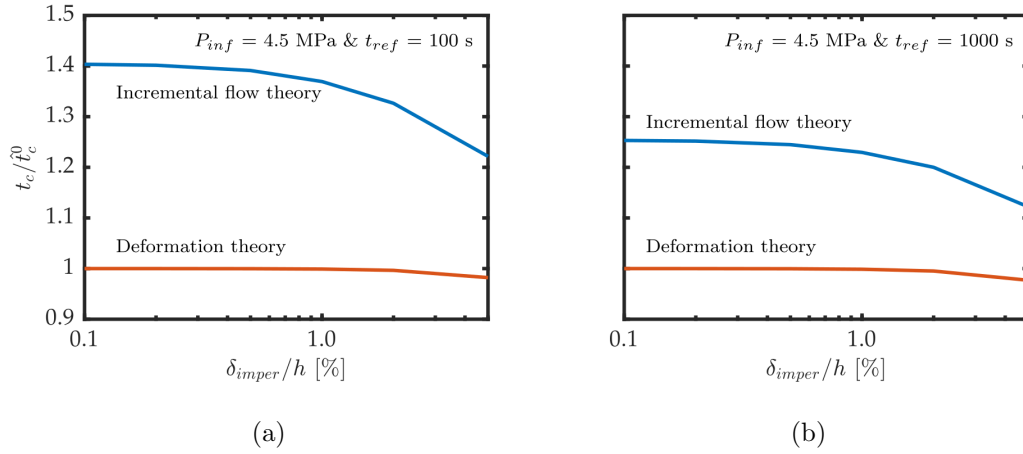
#### 6.1.1. Effect of the geometric imperfections

Because of the geometry of the specimens and their set-up in the test rig, it would have been cumbersome to realise a measurement of the initial egg shape with accuracy. In order to study the effect of initial geometric imperfections on the buckling behaviour of the hemi-egg shells, a numerical analysis was performed.

For the two reference load cases (i.e.  $P_{inf} = 4.5$  MPa and  $t_{ref} = 100$  and  $1000$  s), an initial geometric imperfection was applied to the perfect hemi-egg shell geometry. The imperfection is derived from the first fifteen elastic buckling modes. The amplitude of the imperfection  $\delta_{imper}$  is defined as a fraction of the shell thickness. Different imperfection amplitudes from 0.1 to 5 % of the shell thickness were tested.

The effect of the imperfection amplitude on the critical time was analysed. The results of this analysis are presented in Figure 16. In Figures 16(a) and 16(b), the red curve depicts the evolution of the normalized critical time (i.e.  $t_c/\hat{t}_c^0$ , where  $\hat{t}_c^0$  is the critical time predicted with the deformation theory and the perfect geometry) with respect to the imperfection amplitude. In addition the same analysis was performed using an incremental flow theory. The results for both load cases are depicted by the red curves in Figures 16(a) and 16(b).

Two phenomena can be observed. First, the effect of the initial geometric imperfection on the critical time predicted with the deformation theory is almost negligible as long as the imperfection amplitude is lower than 2% of the thickness. An imperfection amplitude



**Figure 16:** Effect of an initial imperfection on the critical time (a)  $t_{ref} = 100$  s; (b)  $t_{ref} = 1000$  s

equal to 2% of the thickness (i.e. 0.06 mm here) is already important. Moreover, even for an imperfection amplitude equal to 5% of the thickness (i.e. 0.15 mm) the critical time only decreases by few percent.

Then, another classical phenomenon is observed, the critical times predicted with an incremental flow theory tend to converge to the ones from the deformation theory.

Two conclusions can be drawn from these observations. First, the dependency of the structure to the geometric imperfection is only limited. Second, same behaviour as already observed for elasto-plastic materials (cf. [Needleman and Tvergaard \(1982\)](#)) is observed for the elasto-visco-plastic materials.

One can also observe that the results derived from an incremental flow theory do not converge exactly to the ones from the deformation theory. The inaccuracy of the results derived from any incremental flow theory was often explained by the absence of imperfection. It is also one of the most common arguments to discuss the buckling paradox. In this work, we show that the imperfection sensitivity of the structure is not only responsible for the buckling paradox. Even with an important imperfection, the results derived from the incremental flow theory are still far from the predictions with the deformation theory.

### 6.1.2. Effect of the boundary conditions

In this paragraph we intend to evaluate the effect of the boundary condition imperfections on the buckling behaviour of the hemi-egg shell.

In section 5.1.3 a first source of imperfection was identified, i.e. the bending of the specimen holder and the egg flange. It is also very likely that the joint between the egg flange and the hemi-egg shell is not perfectly rigid.

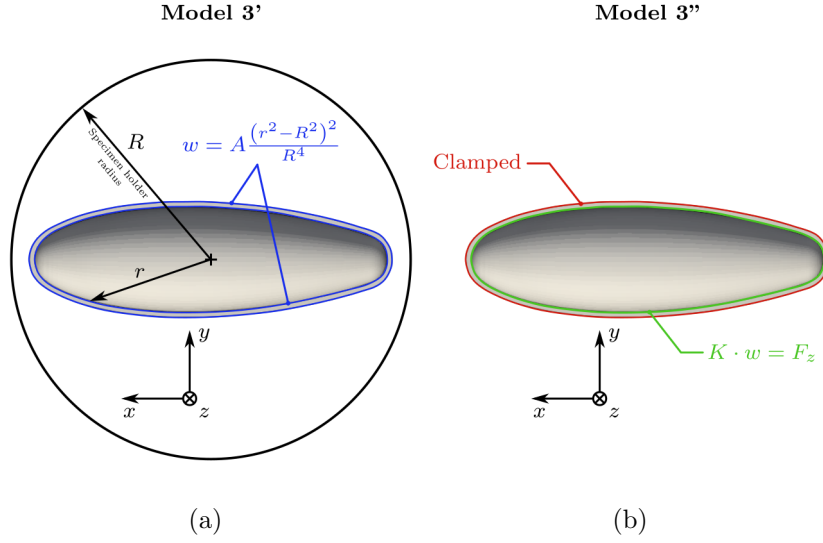
For this purpose the boundary conditions of **Model 2** have been softened. The softening of the boundary conditions are enforced in two additional FE models, **Model 3'** and **Model 3''**, defined as follows:

- **Model 3'**: A displacement field is applied to the edge of hemi-egg shell. This field is derived from the elastic bending of a clamped circular plate:  $w = A(r^2 - R^2)^2 / R^4$ , where  $R$  is the plate radius,  $r$  is the radial coordinate of the current point and  $A$  is the maximum deflection at the center of the plate. In addition,  $A$  is a proportional function of the applied pressure.  $A = A_p \times P$ . As the FE elements are volume shell elements (SHB8PS), the rotations are also constrained.
- **Model 3''**: The edge of the external skin of the hemi-egg shell is perfectly clamped ( $U_x = U_y = U_z = 0$ ). Vertical elastic springs are used on the edge of the inner skin in order to model a rotational elastic stiffness. This allows to model a flexible joint between the hemi-egg shell and its flange.

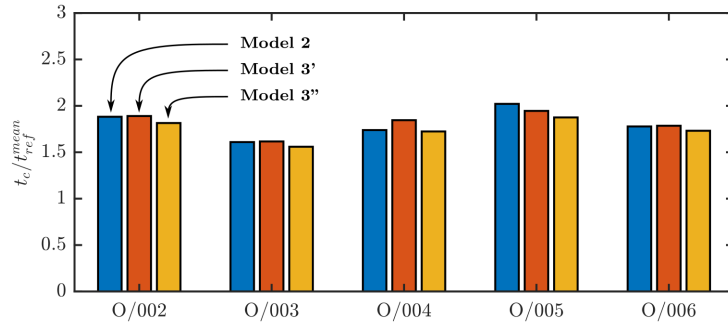
Figure 17 presents both sets of boundary conditions.

To evaluate the two type of boundary condition imperfections, the critical time ratios were predicted for both perturbed boundary conditions as well as for the perfect ones. The predicted critical time ratios are summarised in Figure 18. Blue bars are associated to **Model 2**, the red ones to **Model 3'** and the yellow ones to **Model 3''**. The buckling modes are not affected by perturbed boundary conditions.

As we can notice the predicted critical time ratios evaluated with **Model 3'** (red bars) are generally slightly higher than the ones predicted with **Model 2** (blue bars). Moreover



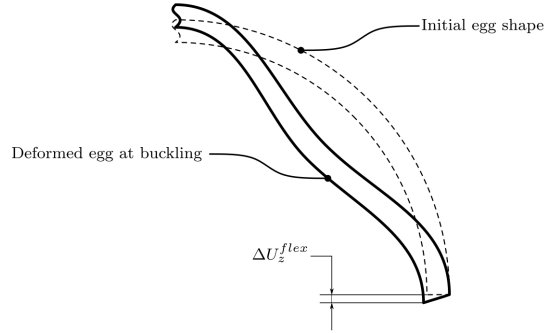
**Figure 17:** (a) Boundary conditions on **Model 3'**; (b) Boundary conditions on **Model 3''**; for **Model 3'**  $A_p = 0.275 \text{ mm.MPa}^{-1}$ ; for **Model 3''**  $K = 2000 \text{ N.mm}^{-1}$



**Figure 18:** Effect of the imperfections on the boundary conditions on the predicted critical time ratio for all specimens

the critical time ratios evaluated with **Model 3''** (yellow bars) are generally lower than the ones predicted with **Model 2**. The hemi-egg shell seems more sensitive to a small flexibility at the flange/egg joint than to the bending of the specimen holder.

In **Model 3''** the flange/egg joint flexibility was magnified. A  $\Delta U_z^{flex}$  at buckling of 0.18 mm was numerically observed between the lower and upper skin edges, as shown in Figure 19. This would correspond to a very flexible material. In reality, the joint is stiffer.



**Figure 19:** Displacement of the edge of the lower skin of **Model 3''** due to the introduced flexibility

It seems that the bending introduced in **Model 3'** stiffens the structure and therefore delays the bifurcation. This is probably due to the compressive axial stress introduced by the bending load. On the other hand, the flexibility introduced in **Model 3''** reduces the critical time ratio as its boundary conditions are more flexible.

In Figure 18 all critical time ratio are very close. It seems that the boundary condition imperfections do not significantly affect the buckling behaviour of the hemi-egg shell structure.

We can conclude that all sources of imperfection identified, either geometric or from the boundary conditions, have a limited impact on the buckling behaviour of the structure. This can be partly explained by the rate dependency of the material. From the buckling experiments, it seems that the rate dependency of the material smooths the imperfection sensitivity on thick structures.

## 6.2. Validation of the buckling prediction model for quasi-proportional loadings

In the previous sections we successively presented the results from the buckling experiments and the ones from the bifurcation analysis. This last paragraph discusses the validity of the buckling prediction model against the experimental results.

As already mentioned in Section 3, all specimens were effectively tested under different testing conditions (cf. Table 4). In order to compare the results from the buckling prediction model with the ones from the experiments, a numerical projection on an ideal testing

condition space was used. It is defined as follows:

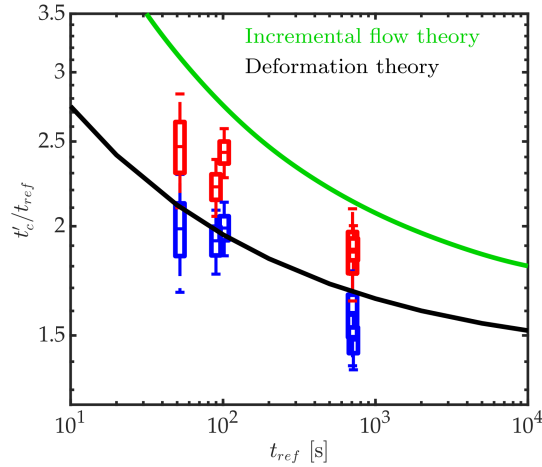
$$r_{t_c} = t_c^{num}(P_{inf}, t_{ref}, R_0) / t_c^{num}(\hat{P}_{inf}, t_{ref}, \hat{R}_0), \quad (17)$$

with  $P_{inf}$ ,  $t_{ref}$  and  $R_0$ , the experimental testing conditions, respectively the saturating pressure, the reference time and the yield stress.  $\hat{P}_{inf}$  and  $\hat{R}_0$  define the ideal testing condition space. Based on the experimental results,  $\hat{P}_{inf} = 4.5$  MPa and  $\hat{R}_0 = 10.4$  MPa.

The projected experimental critical time  $t_c'^{exp}$  is defined as follows:

$$t_c'^{exp} = t_c^{exp} / r_{t_c}. \quad (18)$$

In this way, the experimental critical time ratios from both experimental buckling criteria (i.e. the inversion point and the maximum pressure point) can be compared to the predicted critical values in Figure 20.



**Figure 20:** Comparison of the projected experimental critical time ratios with the predicted critical ratios for both deformation and an incremental flow theories ( $P_{inf} = 4.5$  MPa and  $R_0 = 10.4$  MPa)

In Figure 20 the experimental critical time ratios corresponding to the inversion point are depicted by blue box plots and the ones corresponding to the maximum pressure point are depicted by red box plots. The box plots take into account all experimental discrepancy, i.e.

from the pressure profile and the yield stress identification. They are plotted with respect to the mean reference time.

The predicted critical time ratios (i.e defined through a bifurcation analysis with **Model 1**) are depicted by a black plain curve. They are plotted with respect to the reference time  $t_{ref}$ . Finally, the predicted critical time ratio from an incremental flow theory is also presented in Figure 20 (green plain curve).

One can see that the experimental critical time ratios correlate well with the predictions. The data corresponding to the inversion point seem slightly lower than the predictions, and the ones corresponding to the maximum pressure point are slightly above the prediction. It means that, the model predicts well the buckling of the thick hemi-egg shell.

The difficulty stays in the definition of the experimental buckling. If the buckling is associated to the collapse of the structure (i.e. the maximum pressure point), the prediction model is conservative. If the buckling corresponds to any evidence of buckling initiation (i.e. the inversion point), the model slightly over-estimates the critical time.

Concerning the buckling modes, the model predicts well the proximity of the first two modes as observed experimentally. Moreover, the buckling modes observed experimentally (cf. Figure 8) correlate well with the ones predicted (cf. Figure 13). In addition, it seems that the any source of asymmetrical imperfection leads the structure to buckle on the second mode, except for specimen O/005.

This work shows a good correlation between the experiments and the buckling prediction model. The model developed seems to be relevant for quasi-proportional loadings in the prediction of the critical values as well as the buckling modes.

## 7. Conclusion

A good estimation of the buckling behaviour of the hemi-egg shell was given with the buckling prediction model. The predicted critical values are within the experimental buckling range defined. The predicted buckling modes present similar shapes with the experimental ones.

We also successfully observed symmetrical and asymmetrical buckling modes. It proves experimentally the mode proximity obtained with the numerical model. Even if we observed a low sensitivity of the structure to imperfections either geometric or boundary condition ones, it seems that any source of asymmetrical imperfection forces the structure to buckle on the second mode of the bifurcation analysis.

The experiments were performed for different pressure rates. The predictions show good agreement with experiments for all pressure rates tested. It validates the relevancy of *Bodner's* hypothesis for this shell geometry and these loading cases.

For such a range of conditions, we conclude that the coupling of the deformation theory with *Bodner's* hypothesis predicts well the buckling of hemi-egg shells subjected to external pressure.

The extension of the deformation theory to quasi-proportional loadings for elasto-plastic materials (cf. [Budiansky \(2021\)](#)) was also used with success for elasto-visco-plastic materials. It means that the deformation theory can be used efficiently to predict the buckling of thick elasto-visco-plastic shells subjected to quasi-proportional loadings. In the case of a strongly non-proportional loading, corner theories coupled with *Bodner's* hypothesis could be used.

This work gives an efficient extension to quasi-proportional loadings of the model previously developed in [Jacquet et al. \(2021\)](#). The present method needs to be applied carefully to rate dependent material, as *Bodner's* assumption is mostly limited to low strain rates, otherwise the predictions only allow to obtain a lower bound of the bifurcation point. Moreover, the quasi-proportional loading assumption needs to be assessed carefully as well.

## Acknowledgements

N. Jacquet was supported by a CEA scholarship. N. Jacquet, N. Tardif and T. Elguedj were partially supported by a research contract with CEA. These supports are gratefully acknowledged.



## References

- Abed-Meraim, F., Combescure, A., 2009. An improved assumed strain solid-shell element formulation with physical stabilization for geometric non-linear applications and elastic-plastic stability analysis. *International Journal for Numerical Methods in Engineering* 80, 1640–1686.
- Bardi, F.C., Kyriakides, S., 2006. Plastic buckling of circular tubes under axial compression—part I: Experiments. *International Journal of Mechanical Sciences* 48, 830–841.
- Bodner, S.R., Naveh, M., Merzer, A.M., 1991. Deformation and buckling of axisymmetric viscoplastic shells under thermomechanical loading. *International Journal of Solids and Structures* 27, 1915–1924.
- Budiansky, B., 2021. A Reassessment of Deformation Theories of Plasticity. *Journal of Applied Mechanics* 26, 259–264.
- CEA, 2018. Cast3M.
- Christoffersen, J., Hutchinson, J.W., 1979. A class of phenomenological corner theories of plasticity. *Journal of the Mechanics and Physics of Solids* 27, 465–487.
- Combescure, A., Jullien, J.F., 2017. Creep buckling of cylinders under uniform external pressure: Finite element simulation of buckling tests. *International Journal of Solids and Structures* 124, 14–25.
- Dompierre, B., Aubin, V., Charkaluk, E., Filho, W.C.M., Brizoux, M., 2011. Cyclic mechanical behaviour of Sn3.0Ag0.5Cu alloy under high temperature isothermal ageing. *Materials Science and Engineering: A* 528, 4812–4818.
- Eslami, M.R., Shariyat, M., 1997. Elastic, Plastic, and Creep Buckling of Imperfect Cylinders Under Mechanical and Thermal Loading. *Journal of Pressure Vessel Technology* 119, 27–36. Publisher: American Society of Mechanical Engineers Digital Collection.
- Gerard, G., Gilbert, A.C., 1958. A Critical Strain Approach to Creep Buckling of Plates and Shells. *Journal of the Aerospace Sciences* 25, 429–434.
- Hughes, T.J., Shakib, F., 1986. Pseudo-corner theory: a simple enhancement of J2-flow theory for applications involving non-proportional loading. *Engineering Computations* 3, 116–120.
- Hutchinson, J.W., 1974. Plastic Buckling, in: Yih, C.S. (Ed.), *Advances in Applied Mechanics*. Elsevier. volume 14, pp. 67–144.
- Jacquet, N., 2021. Elasto-visco-plastic buckling of thick shells. phdthesis. Université de Lyon.
- Jacquet, N., Tardif, N., Elguedj, T., Garnier, C., 2021. Numerical study and experiments on the elasto-visco-plastic bifurcation buckling of thick anisotropic plates. *Thin-Walled Structures* 166, 108070.
- Kim, K.S., Huh, S.H., Suganuma, K., 2002. Effects of cooling speed on microstructure and tensile properties of Sn–Ag–Cu alloys. *Materials Science and Engineering* 333, 106–114.
- Kyriakides, S., Bardi, F.C., Paquette, J.A., 2005. Wrinkling of Circular Tubes Under Axial Compression: Effect of Anisotropy. *Journal of Applied Mechanics* 72, 301–305.

- Mikkelsen, L.P., 1993. On the analysis of viscoplastic buckling. *International Journal of Solids and Structures* 30, 1461–1472.
- Needleman, A., Tvergaard, V., 1982. Aspects of Plastic Postbuckling Behavior, in: Hopkins, H.G., Sewell, M.J. (Eds.), *Mechanics of Solids*. Pergamon, Oxford, pp. 453–498.
- Paley, M., Aboudi, J., 1991. Viscoplastic bifurcation buckling of plates. *AIAA Journal* 29, 627–632.
- Papirno, R., Goldman, R., 1969. Experimental creep buckling of aluminum cylinders in axial compression. *Experimental Mechanics* 9, 356–365.
- Réthoré, J., 2018. Ufreckles.
- Sammari, A., Jullien, J.F., 1995. Creep buckling of cylindrical shells under external lateral pressure. *Thin-Walled Structures* 23, 255–269.
- Simo, J.C., 1987. A J2-flow theory exhibiting a corner-like effect and suitable for large-scale computation. *Computer Methods in Applied Mechanics and Engineering* 62, 169–194.
- Triantafyllidis, N., Massin, P., Leroy, Y.M., 1997. A sufficient condition for the linear instability of strain-rate-dependent solids. *Comptes Rendus de l'Académie des Sciences - Series IIB - Mechanics-Physics-Chemistry-Astronomy* 324, 151–157.
- Tvergaard, V., 1983. Plastic buckling of axially compressed circular cylindrical shells. *Thin-Walled Structures* 1, 139–163.
- Tvergaard, V., Needleman, A., 2000. Buckling localization in a cylindrical panel under axial compression. *International Journal of Solids and Structures* 37, 6825–6842.
- Yeh, M.K., Kyriakides, S., 1986. On the Collapse of Inelastic Thick-Walled Tubes Under External Pressure. *Journal of Energy Resources Technology* 108, 35–47.
- Zhang, J., Wang, M., Wang, W., Tang, W., 2017. Buckling of egg-shaped shells subjected to external pressure. *Thin-Walled Structures* 113, 122–128.